Supporting Information

$CsPbBr_3$ nanocrystals supported on partially oxidized Ti_2N MXenes for photothermal CO_2 conversion

Kevin Mego[1]*, Emanuela Accardo*[2]*, Pedro Ruiz-Campos*[3]*, Herme G. Baldoví*[2]** and Pedro Atienzar*[1]***

[1] Instituto de Tecnología Química, Consejo Superior de Investigaciones Científicas, Universitat Politècnica de València, Avenida de los Naranjos s/n, 46022 Valencia, Spain

[2] Departamento de Química, Universitat Politècnica de València, Camino de Vera s/n, 46022 Valencia, Spain

[3] Universidad Científica del Sur, Panamericana Sur Km 19, 150142 Lima, Perú

Corresponding author: Pedro Atienzar (pedatcor@itq.upv.es) | Hermenegildo García Baldoví (hergarba@itq.upv.es)

Keywords: photocatalysis, perovskites, partially oxidized MXenes, charge transfer

SUMMARY:

1. Materials and Methods

1.1. Chemicals

The chemicals listed below were obtained from commercial suppliers and used as received without additional purification.

Reagents: cesium carbonate (Cs_2CO_3, Sigma-Aldrich, 90%), lead (II) bromide ($PbBr_2$, Thermo Fisher Scientific, 99.9%), titanium aluminum nitride MAX phase (Ti_3AlN, Nanochemazone, 99%), cooper (II) chloride ($CuCl_2$, Sigma-Aldrich, 99%), potassium persulfate (KPS, Sigma-Aldrich, 99%).

Solvents: oleic acid (OA, Sigma-Aldrich, 90%), oleylamine (OLA, Sigma-Aldrich, 70%), 1-octadecene (ODE, Sigma-Aldrich, 90%), tert-butanol (Sigma-Aldrich, 99%) n-hexane (Panreac, 95%).

1.2. Characterization techniques

The phase composition of the samples was determined by powder X-ray diffraction (PXRD) on a Philips XPert diffractometer operating at 40 kV and 45 mA, with Ni-filtered Cu Kα radiation. Thermogravimetric analyses (TGA) were conducted using a TGA/DSC3+ station from METTLER TOLEDO. The microstructure and morphology were observed through transmission electron microscopy (TEM) and dark-field scanning transmission electron microscopy (DF-STEM) on a JEOL JEM-2100F instrument operating at 200 kV. The chemical composition and surface states of the samples were examined by X-ray photoelectron spectroscopy (XPS) using a SPECS spectrometer with an MCD-9 detector and a monochromatic Al Kα (1486.6 eV) X-ray source; the C 1s peak at 284.8 eV served as the reference binding energy, and CASA software was utilized for spectral deconvolution. The optical properties, including absorption and reflection spectra, were obtained by UV-Vis-NIR diffuse reflectance spectroscopy using an Agilent Cary 7000 spectrophotometer. Nuclear magnetic resonance (NMR, ^{1}H,^{13}C) spectra were recorded using a Bruker Ascend 400 MHz NMR spectrometer to analyze the molecular structure of the samples. Steady-state PL measurements were recorded in an Edinburgh Instruments FLS1100 spectrofluorometer using a 450 W xenon lamp light equipped with a double monochromator for excitation and emission coupled to a cooled photomultiplier (PMT-980). Lifetime measurements were performed using the FLS1100 spectrofluorometer with a pulsed LED as an excitation source (405 nm) and a Time-Correlated Single Photon Counting (TCSPC) as a detector.

Moreover, H_2 temperature-programmed reduction (H_2-TPR) was employed to assess the reducibility of Ti_2N MXene/TiO_2 species. The analysis was conducted by using an AutoChem

2920 chemisorption unit (Micromeritics, Atlanta, USA). In this method, a fixed amount of the catalyst sample was placed on a thin quartz wool bed within a U-shaped tubular reactor. The catalyst was initially subjected to oxidation by passing argon gas at a temperature of 100 °C for 30 min. Subsequently, the catalyst underwent purging and cooling steps under pure He gas (with a purity level of $\geq$ 99.999 %). Following the initial steps, the catalyst sample was subjected to a controlled reduction process. A gas mixture comprising 10 vol% H_2 in Ar was introduced, and the temperature was progressively increased from ambient to 800 °C at a controlled rate of 10 $°C \cdot min^{-1}$. Throughout this process, the consumption of H_2 was continuously monitored using a thermal conductivity detector (TCD).

CO_2-TPD measurements were performed using a Micromeritics AutoChem 2920 instrument on powdered samples. The system was pre-treated by purging with helium at a temperature of 200°C under continuous flow of He. Once the sample cooled, a gas mixture containing 5 vol% CO_2 in Ar was introduced for 30 minutes to allow surface saturation. Following the adsorption step, the gas was switched back to helium, and the desorption profile was recorded by ramping the temperature at a rate of 10 $°C \cdot min^{-1}$ up to 800 °C. CO_2 desorption was monitored continuously using a TCD.

1.3. Procedures

1.3.1. Synthesis of Cesium Oleate (CsOL)

Using a 1:3 Cs:OA ratio as an example, Cs_2CO_3 (0.192 g, 1 mmol) was mixed with OA (2.4 mL, 3 mmol), and ODE (40mL, 50mmol). The sample was heated in a three-neck flask under continuous stirring using a magnetic stir bar at 110 °C for half an hour under vacuum and placed under argon at 110 °C for 1 hour until no visible bubbles were observed. Note that the sample was placed under vacuum slowly to avoid vigorous removal of volatile carbon dioxide and water vapor generated during the reaction. Then, the temperature was increased to 150 °C for an additional hour, until all the cesium salt was completely dissolved. Once the reaction was completed, the system was allowed to cool to room temperature, yielding cesium oleate (CsOL). The sample was stored in a refrigerator until the next reaction.[1]

To obtain pure CsOL, the previous suspension will be filtered to separate the solid of interest from the excess supernatant (OA + ODE). The resulting solid will be washed with ether (4x30 mL) and dried under vacuum overnight. The final product, pure CsOL, is a yellowish waxy solid, and its structure will be confirmed by ^{1}H-NMR (Figure S1, S2).

Equation 1 describes the acid metathesis reaction, which involves the ion exchange between cesium carbonate and oleic acid. Cesium carbonate provides cesium cations that combine with the oleate anions from oleic acid. This process results in the formation of clear cesium oleate upon complete conversion.

$$Cs_2CO_3 + 2RCOOH \leftrightharpoons 2CsOOR + H_2O\uparrow + CO_2\uparrow \tag{1}$$

$R = C_{17}H_{33}$

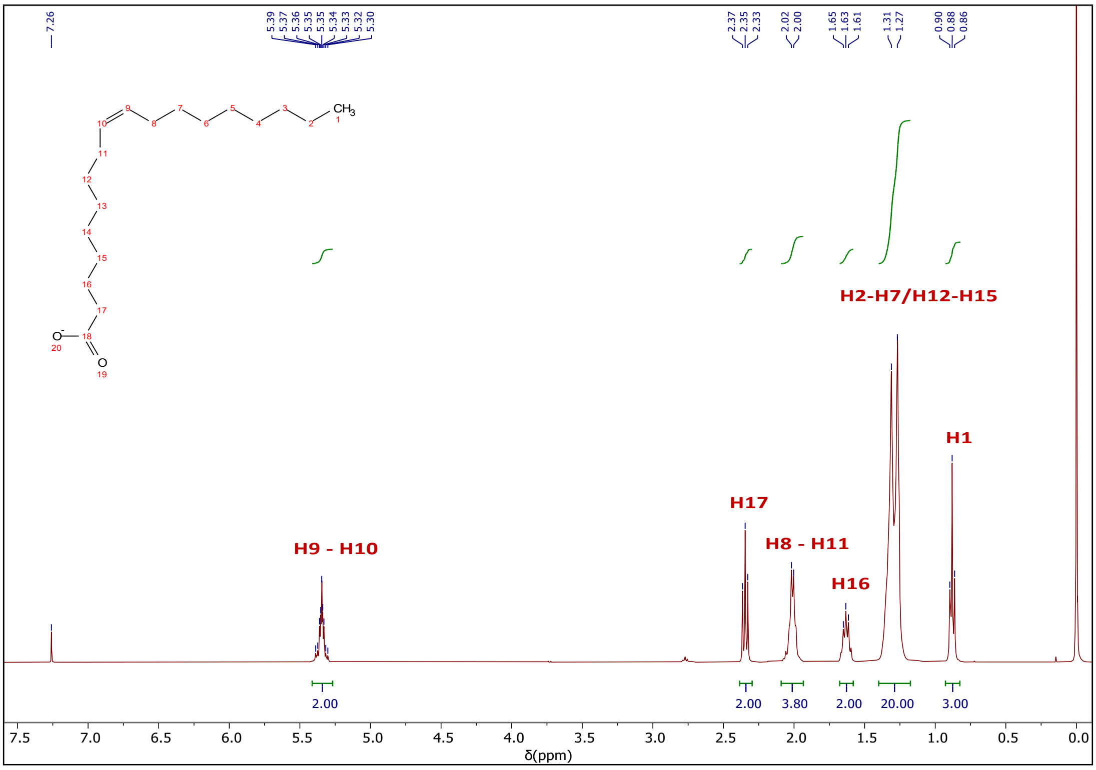

Figure S1. ^{1}H-NMR spectrum for pure CsOL with H integration.

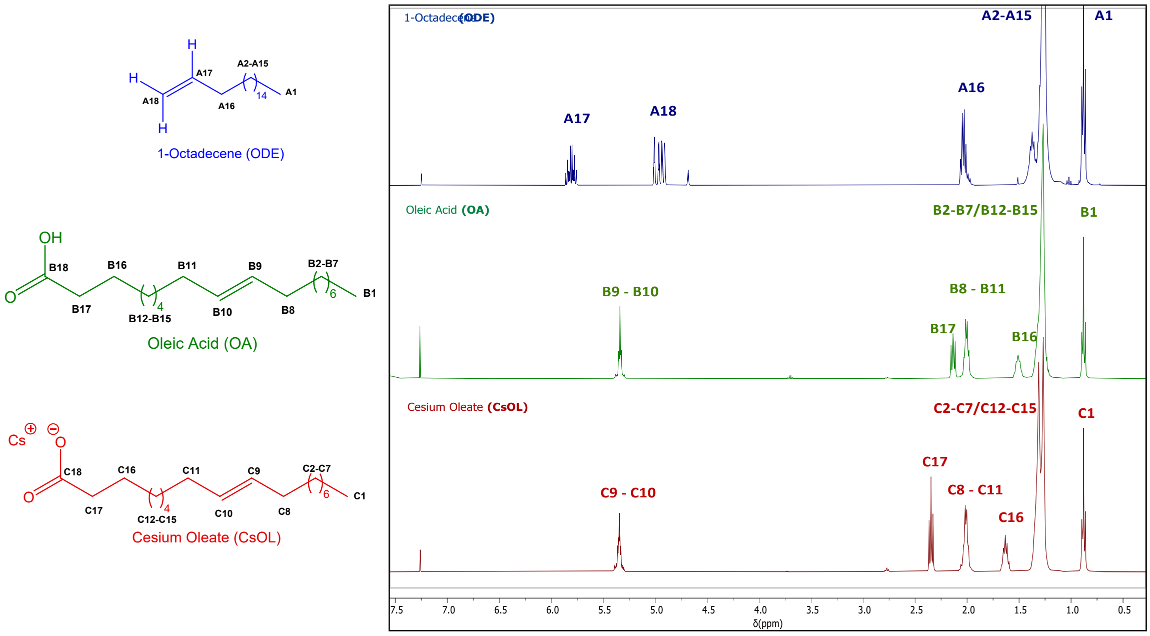

Figure S2. Comparison of ^{1}H-NMR results for ODE (blue), OA (green) and CsOL (red).

1.3.2. Synthesis of perovskite $CsPbBr_3$ NCs

$PbBr_2$ (138 mg, 0.37 mmol) is added to a three-neck round-bottom flask along with ODE (10 mL, 30.9 mmol). The solution is placed under vacuum, and the temperature is gradually increased to 120 °C over 1 hour to eliminate traces of water molecules that may be present in ODE and to prevent their condensation during the reaction. The system is then switched to an argon atmosphere. Subsequently, to dissolve the $PbBr_2$, OA (1 mL, 3.15 mmol) and OLA (1 mL, 3.10 mmol) are loaded into two separate syringes and added while maintaining the temperature at 120 °C.

Once the $PbBr_2$ solution is obtained, the reaction temperature is increased to 190 °C, followed by a rapid injection of CsOL (1 mL, 0.11 mmol), which must be preheated to 120 °C. After 5 seconds, the flask is immersed in an ice bath to halt the growth of the $CsPbBr_3$ NCs.[1] The $CsPbBr_3$ NCs from the reaction are allowed to cool to room temperature, and this crude solution is collected in a 20 mL conical centrifuge tube. Then, 10 mL of tert-butanol is added, and the mixture is centrifuged at 8000 rpm for 10 minutes. The supernatant, containing excess ligand and unreacted starting materials, is discarded, and the precipitate is dispersed in 5 mL of hexane. This mixture is centrifuged again at 8000 rpm for 10 minutes (this process is repeated 2 times). Finally, the obtained precipitate is redispersed in 4 mL of hexane and stored in a refrigerator.

The chemical reaction that leads to the formation of the $CsPbBr_3$ phase is given by equation 2.

$$3PbBr_2 + 2CsOOR \longrightarrow 2CsPbBr_3 + Pb(OOR)_2 \qquad \textbf{(2)}$$

$R = C_{17}H_{33}$

1.3.3. Synthesis of Ti_2N MXene (molten salt method)

In a dry box, Ti_3AlN MAX phase and $CuCl_2$ were mixed in a 1:5 molar ratio to ensure a precise stoichiometric reaction. The resulting mixture was then transferred to a crucible and placed in an oven. Utilizing the molten salt method, the mixture was heated to 650 °C for 8 hours under an argon atmosphere. In this process, $CuCl_2$ acts as a Lewis acid, facilitating the etching.[2]

After the heating process, the solid product was recovered and subjected to a purification step. The solid was purified using a 0.4M solution of potassium persulfate (KPS) at 70 °C for 2 hours and 30 minutes. This purification step is critical to remove excess copper from the surface of the MXene.

Following the purification, the mixture was filtered under vacuum to efficiently separate the solid from the liquid phase. The solid residue was then dried thoroughly to remove any remaining solvent.

1.3.4. Preparation of $CsPbBr_3$@Ti_2N MXene

Following the perovskite synthesis, previously synthesized Ti_2N MXene was dispersed in hexane (0.3 mg/mL). MXene was exfoliated using pulsed sonication (1s on/1s off) at the 31% amplitude setting, for 3 hours in an ultrasonic tip.

Subsequently, $CsPbBr_3$ nanocrystals (5% wt.) were added to the MXene solution. To achieve a suitable suspension of perovskite nanocrystals on MXene, the mixture was sonicated in an ultrasonic bath for 1 hour, the solvent was evaporated at room temperature and the solid obtained was dried under vacuum. The sonication process not only promoted the dispersion of nanocrystals but also induced the formation of defects and surface oxygenated functional groups in MXene. These defects and functional groups are expected to enhance non-covalent interactions, such as Van der Waals forces and hydrogen bonds, with the cesium perovskite nanocrystals.

The presence of defects in MXene is particularly advantageous for catalytic applications, such as the Sabatier reaction for CO_2 methanation. These defects can serve as active sites for catalyzing the conversion of CO_2 to methane, thereby improving the catalytic performance of the newly formed material.

1.3.5. Photocatalytic CO_2 reduction test

In a typical test, the photocatalytic methanation of CO_2 was carried out using a quartz photoreactor (41 mL) equipped with two stainless steel fittings. One fitting was provided with a needle for gas introduction to purge the reactor system, and the other was equipped with a pressure gauge (Swagelok 316 SS) to measure the internal pressure of the system. Additionally, a heating plate was used to control the system temperature (Figure S3). Briefly, 10 mg of the $CsPbBr_3$@Ti_2N MXene catalyst powder, which had been previously dried under vacuum for 12 hours, was introduced into the photoreactor. The system was then purged with H_2 for 15 minutes, after which CO_2 was introduced into the photoreactor until achieving a H_2:CO_2 molar ratio of 4:1 and a final pressure of 1.50 bar. Subsequently, the photoreactor was heated to various temperatures (160, 180, 200, 220, and 250 ºC) and then irradiated using a commercially available Hg-Xe lamp (150 W, Hamamatsu ref. L8253, equipped with an optical fiber A10014-50-0110; Figure S3) with simulated sunlight (226 $mW \cdot cm^{-2}$) for 23 hours. The irradiances were measured using a commercially available photodiode (optical power meter 843-R; Newport Corporation).[3]

Control experiments were conducted using either the $CsPbBr_3$ NC and the POM-Ti_2N MXene alone, both of which showed significantly lower methane production compared to the combination of both catalysts ($CsPbBr_3$@POM-Ti_2N MXene). Furthermore, experiments were performed under both dark conditions and simulated sunlight to discern whether the observed photocatalytic activity was primarily due to thermal effects or photothermal effects.

At the designated reaction time, aliquot samples were collected from either the continuous flow or batch photoreactor. These samples were then analyzed using an Agilent 490 MicroGC system, which is equipped with two analytical channels and thermal conductivity detectors. The first channel, equipped with a MolSieve 5Å column, allowed for the precise separation and detection of small molecules such as H_2, O_2, N_2, and CO. The second channel, which housed a Pore Plot Q column, was utilized to accurately identify and quantify CO_2, CH_4, and short-chain hydrocarbons. Quantitative analysis was carried out by comparing the sample measurements to calibration curves that were established using commercially available gas standards, ensuring the reliability and accuracy of the photocatalytic reaction product measurements.

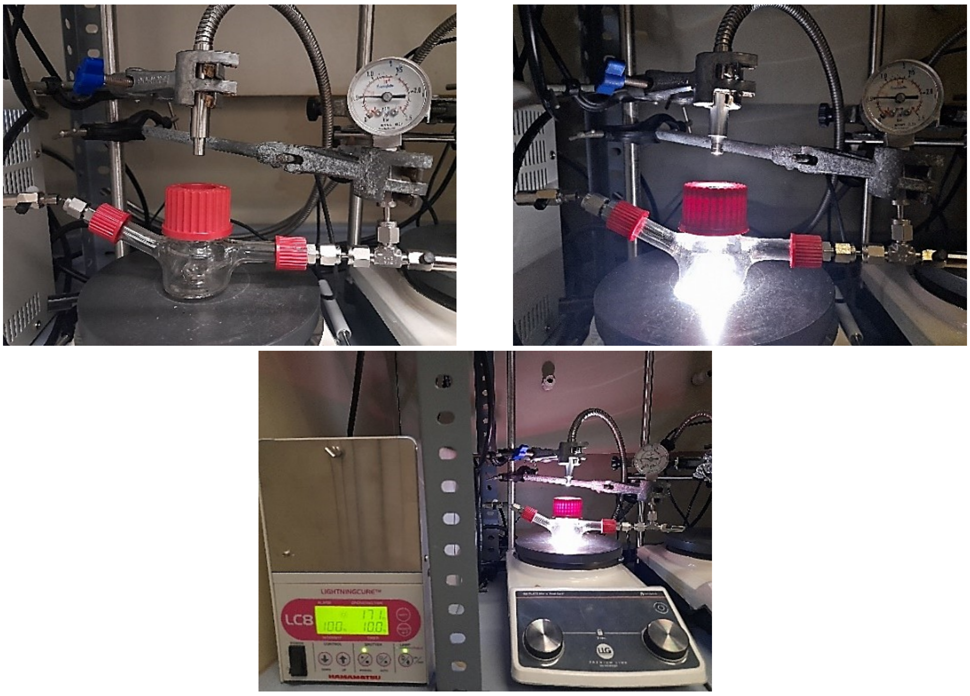

Figure S3. Custom-designed reactor setup for photocatalytic CO_2 reduction. The system employs a mercury-xenon lamp (150 W, Hamamatsu model L8253) equipped with an optical fiber (model A10014-50-0110) to simulate sunlight at an intensity of 226 $mW \cdot cm^{-2}$. The reactor features a custom glass container with three necks, allowing for controlled gas flow and sampling. A cup-shaped well at the base of the reactor focuses the simulated sunlight directly onto the sample, ensuring precise and uniform light exposure.

1.3.6. Computational Details

All periodic DFT calculations were carried out with VASP 6.4.2 using the PAW method and the PBE generalized-gradient approximation for the exchange-correlation functional. Dispersion interactions were described by the D3(BJ) correction (IVDW = 12). PAW pseudopotentials of the PBE type were employed for all atoms (Ti_pv for Ti, and standard PBE PAWs for N, O, C and H). A kinetic-energy cutoff of 520 eV and PREC = Accurate were used in all cases. Electronic self-consistency was converged to 10^{-6} eV for geometry optimizations and to 10^{-7} eV for the final single-point energy calculations. Non-spherical contributions inside the PAW spheres were included (LASPH = .TRUE.), real-space projection was disabled (LREAL = .FALSE.), and a finer FFT grid was employed (ADDGRID = .TRUE.). Symmetry was switched off for all slab calculations (ISYM = 0).

Slab models of Ti_2N MXene, TiN (100) and rutile TiO_2 (110) (with and without a surface oxygen vacancy) were constructed with vacuum regions of approximately 15 - 18 Å along the surface normal and corrected for spurious dipole interactions (LDIPOL = .TRUE., IDIPOL = 3). Monkhorst–Pack k-point grids commensurate with the supercell size were employed. The Ti_2N MXene was modelled as a 3x3 supercell of a single Ti-N-Ti trilayer ($Ti_{18}N_9$). The TiN support was described by a rock-salt TiN (100) slab. Rutile TiO_2(110) was represented by a 2x2 surface supercell; the pristine slab contained 16 Ti and 36 O atoms, and the defective slab contained 16 Ti and 35 O atoms after removal of one surface O atom to create a V_O.

Geometry optimizations were carried out by relaxing ionic positions at fixed cell (ISIF = 2). For Ti_2N MXene and TiN (100), non-spin-polarized calculations (ISPIN = 1) with metallic smearing (ISMEAR = 1, SIGMA = 0.20 eV) were used, together with Monkhorst–Pack k-point meshes of 5x5x1 (Ti_2N) and 3x3x1 (TiN). For TiO_2 (110) (both pristine and V_O), spin-polarized calculations were employed (ISPIN = 2) with initial local moments on Ti (MAGMOM = 16*1.0 36*0.0 for the pristine slab and 16*1.0 35*0.0 for the V_O slab), and Gaussian smearing appropriate for oxides (ISMEAR = 0, SIGMA = 0.05 eV), using a Γ-centered 3x6x1 k-point grid. Forces were relaxed below 0.01–0.02 eV $Å^{-1}$ (as set by EDIFFG) using IBRION = 2 (conjugate-gradient) for Ti_2N/TiN and IBRION = 1 (quasi-Newton) for TiO_2.

For each converged structure, a high-precision single-point energy calculation was performed with NSW = 0, IBRION = -1, EDIFF = 10^{-7} eV, and the same functional, cutoff, dispersion scheme, vacuum thickness, dipole correction and k-point mesh as in the corresponding geometry optimization. For Ti_2N and TiN, non-spin-polarized single-point calculations with small Gaussian smearing (ISPIN = 1, ISMEAR = 0, SIGMA = 0.05 eV) were used consistently for the clean slab, the slab+adsorbate, and the isolated molecule. For TiO_2, the spin-polarized setup and ISMEAR = 0, SIGMA = 0.05 eV were retained, together with the same MAGMOM pattern used in the relaxations.

1.3.6.1. Adsorption energy calculations

Reference energies for gas-phase H_2 and CO_2 were obtained from DFT calculations in large cubic cells (15 - 20 Å) using the same PBE-D3(BJ) setup, Γ-point sampling and Gaussian smearing (ISMEAR = 0, SIGMA = 0.05 eV), with full optimization of molecular geometries. For each surface and molecule, the electronic adsorption energy was computed as:

$$E_{ads} = E_{slab+mol} - E_{slab} - E_{mol_{(gas)}} \tag{3}$$

where $E_{slab+mol}$ is the total energy of the relaxed slab with the adsorbed molecule, E_{slab} is <<the energy of the corresponding clean slab, and $E_{mol(gas)}$ is the energy of the isolated gas-phase molecule. By this convention, negative values indicate exothermic adsorption. The numerical values cited in the main article had been collected in Table S1.

System	Configuration	E_{ads} (eV)	E_{ads} (kcalmol^{-1})	Geometry notes
Ti_2N MXene	H_2 (molecular)	-0.04	-0.98	H_2 linear, far from surface
Ti_2N MXene	H_2 (dissociated)	-7.57	-174.54	Two H atoms bound to surface sites
Ti_2N MXene	CO_2 (molecular)	-3.32	-76.47	CO_2 bent, chemisorbed on Ti/N
TiO_2 (110)	CO_2 (molecular)	-0.10	-2.21	Tilted CO_2 to surface sites
TiO_2 (110) + V_O	CO_2 (molecular)	-1.11	-25.50	CO_2 bound at vacancy site
TiN (100)	H_2 (molecular)	6.71	154.85	No bound state; H_2 repelled

Table S1. Calculated adsorption energies (E_{ads}) and key structural features for H_2 and CO_2 on Ti_2N MXene, TiN (100) and TiO_2 (110) surfaces.

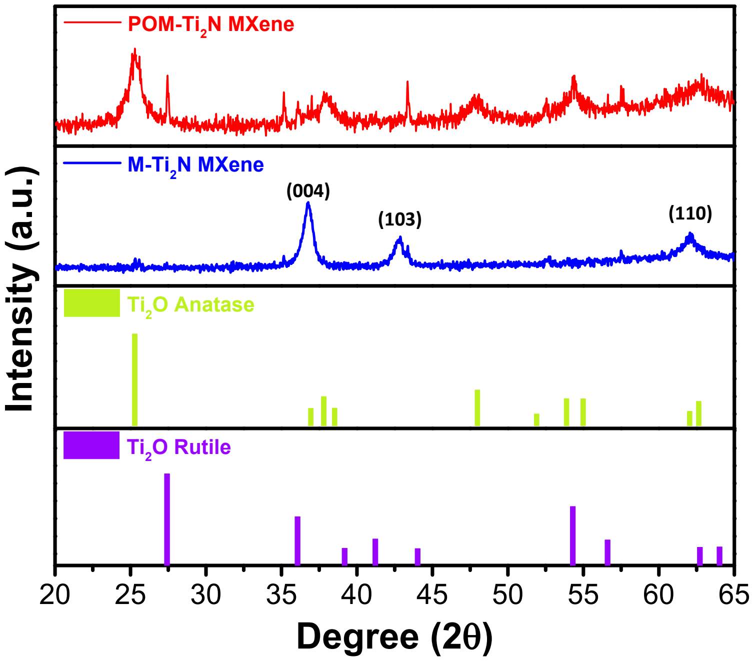

Figure S4. X-ray diffractogram of M-Ti$_2$N MXene (blue) and POM-Ti$_2$N MXene (red). The diffraction lines for common titanium oxide impurities, anatase (ICSD #9852[4], green) and rutile (ICSD #9161[5], violet), are provided as references to confirm the phase purity of the synthesized MXenes.

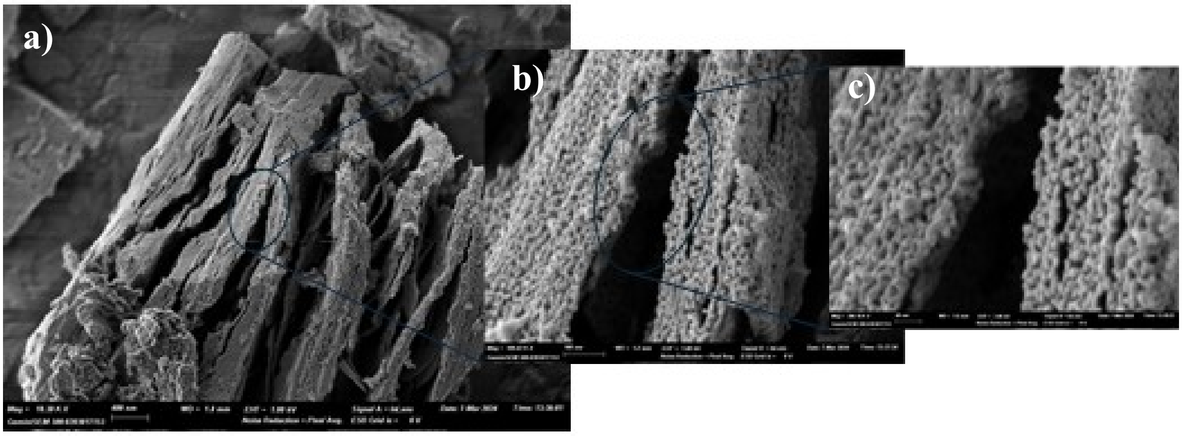

Figure S5. a) HR-FESEM image of a particle of POM-Ti$_2$N, and b) and c) zooms of the multilayer structure.

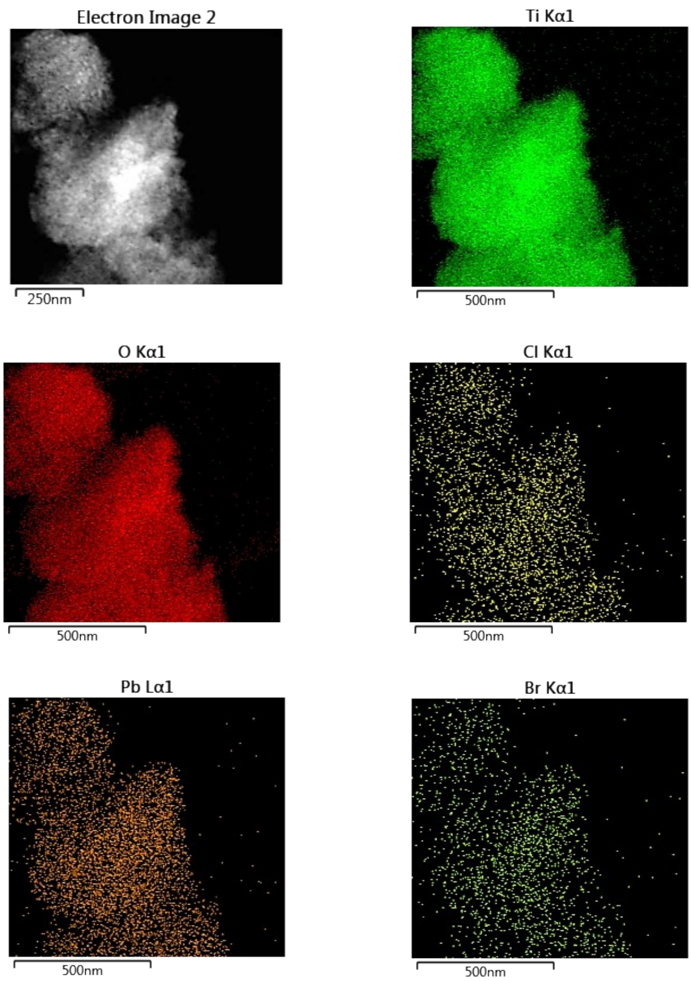

Figure S6. DF-STEM images of the composite $CsPbBr_3$@POM-Ti_2N.

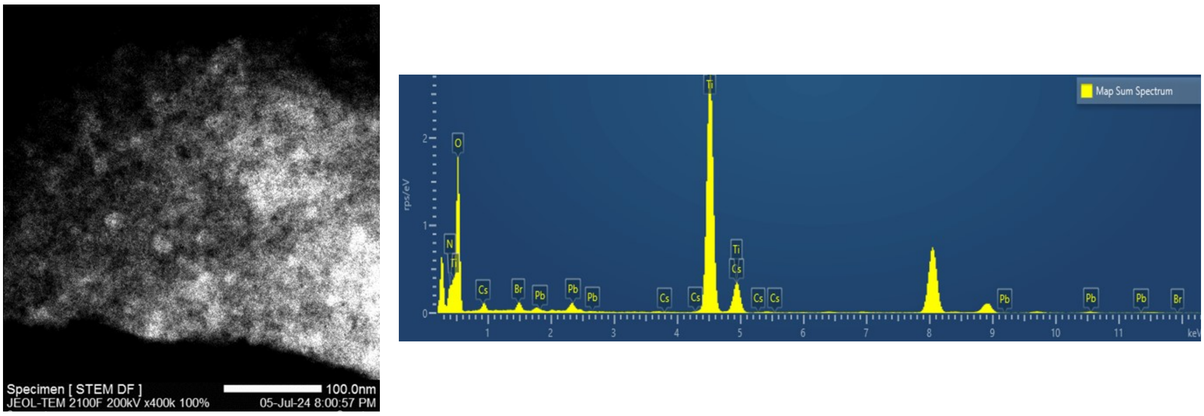

Figure S7. STEM-EDS elemental mapping and corresponding EDS spectrum of the $CsPbBr_3$@POM-Ti_2N hybrid material. The dark-field STEM image (left), while the EDS spectrum (right) confirms the presence of the constituent elements: Cs, Pb, Br (perovskite), and Ti, N, O (POMXene).

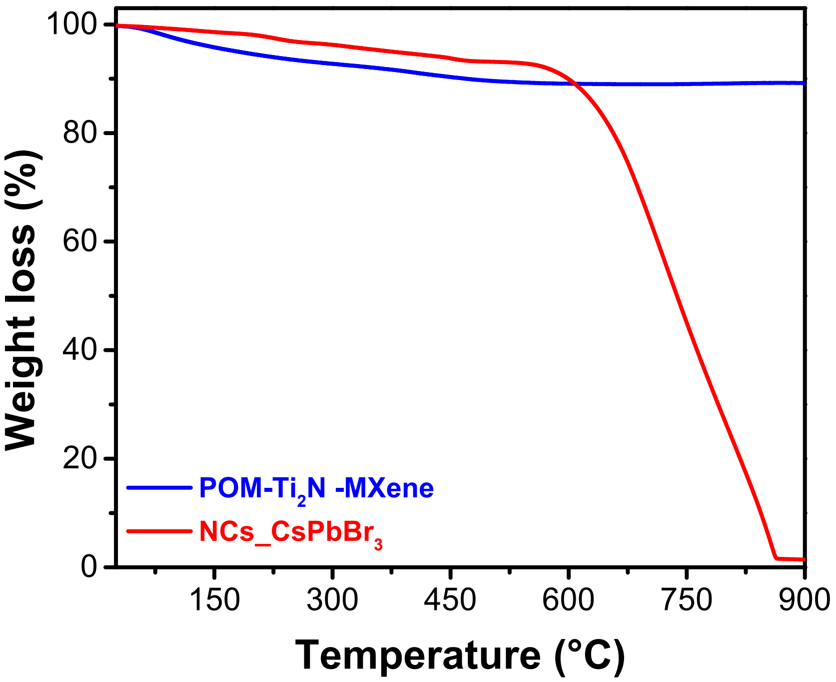

Figure S8. TGA of NCs_CsPbBr$_3$ (red line), POM-Ti$_2$N-MXene (blue line).

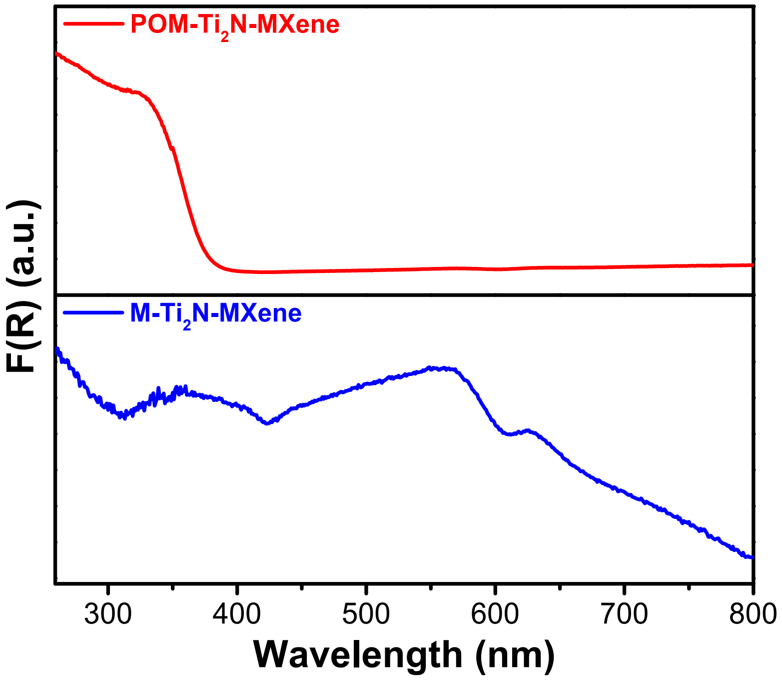

Figure S9. UV-Vis spectrum of M-Ti$_2$N MXene (blue line) and POM-Ti$_2$N MXene (red line).

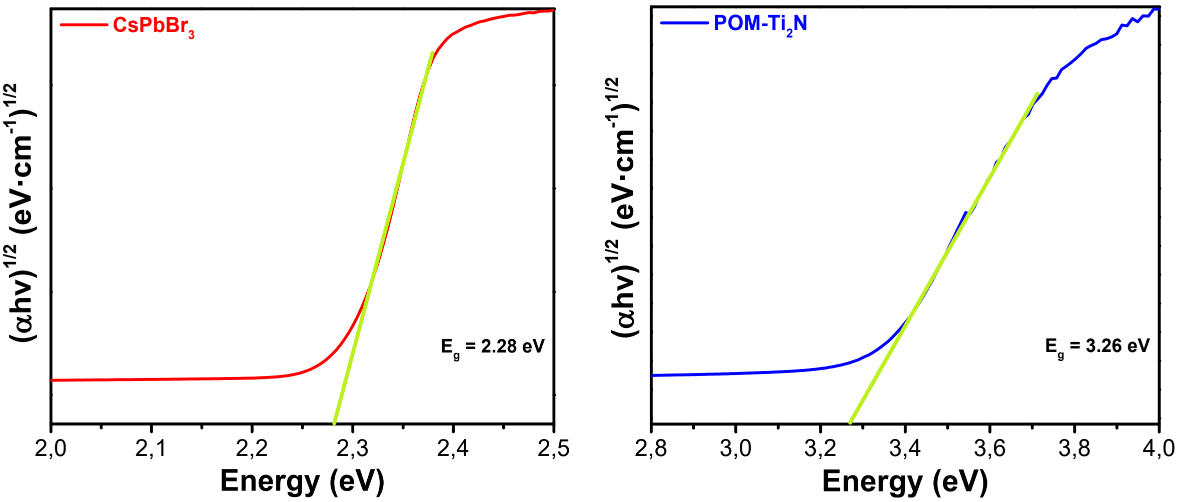

a) b)

Figure S10. Optical bandgap of a) $CsPbBr_3$ NCs and b) POM-Ti_2N. Green lines indicate optical bandgaps determined from Tauc plots.

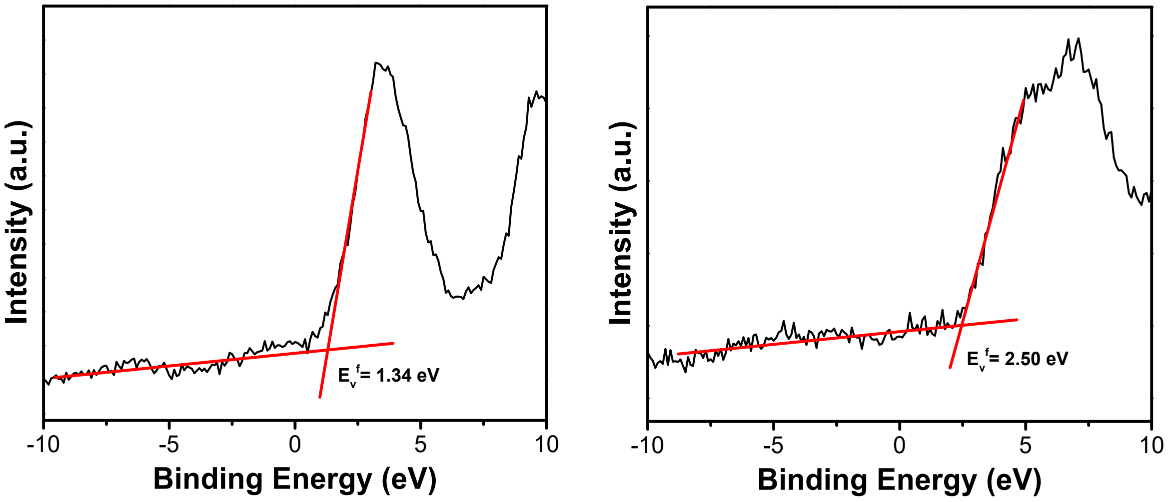

a) b)

Figure S11. X-ray photoelectron spectra of a) $CsPbBr_3$ NCs and b) POM-Ti_2N, to calculate the valence band maximum.

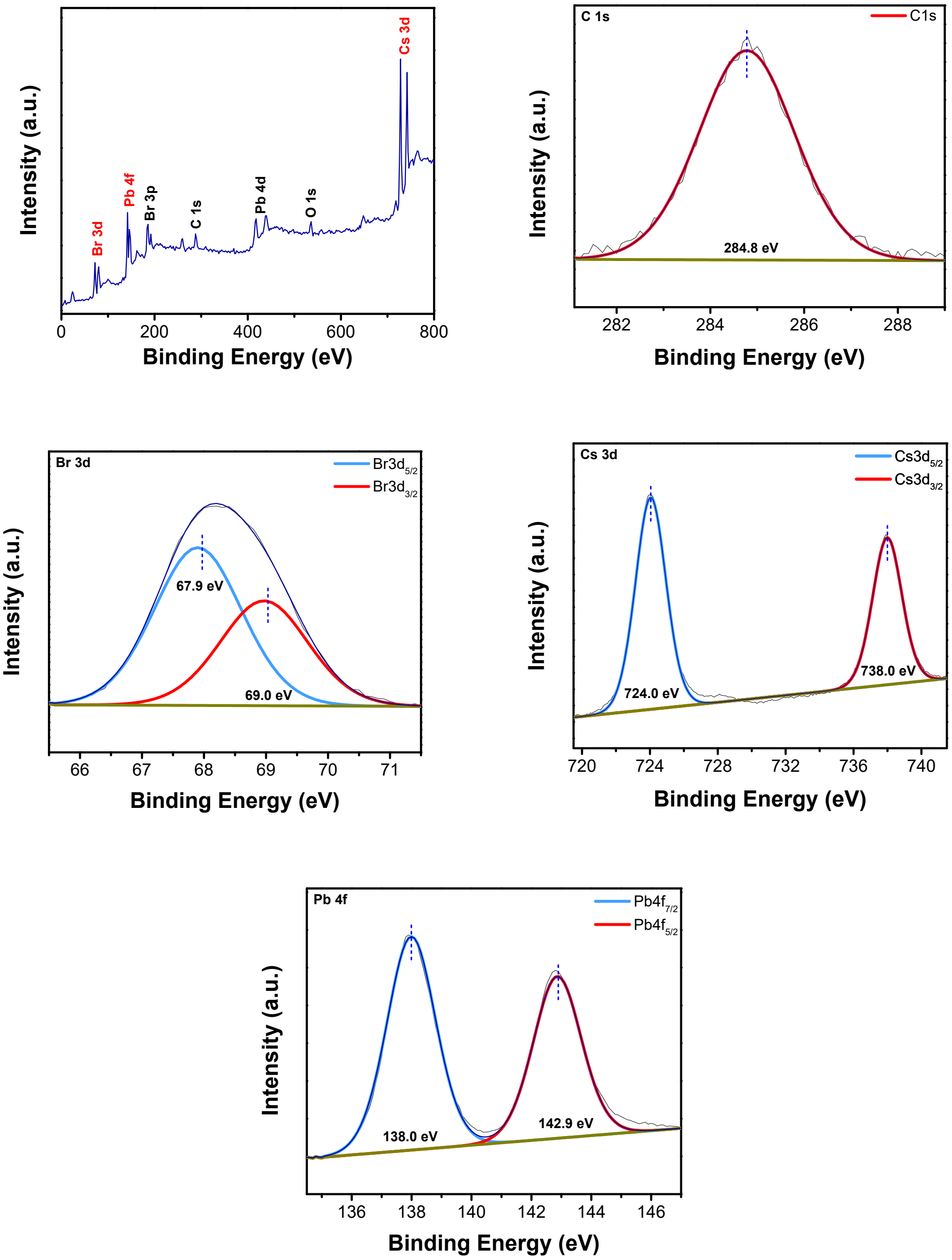

Figure S12. XPS spectra of $CsPbBr_3$ NCs powders. High-resolution XPS spectra of survey, C1s, Br3d, Cs3d and Pb4f respectively.

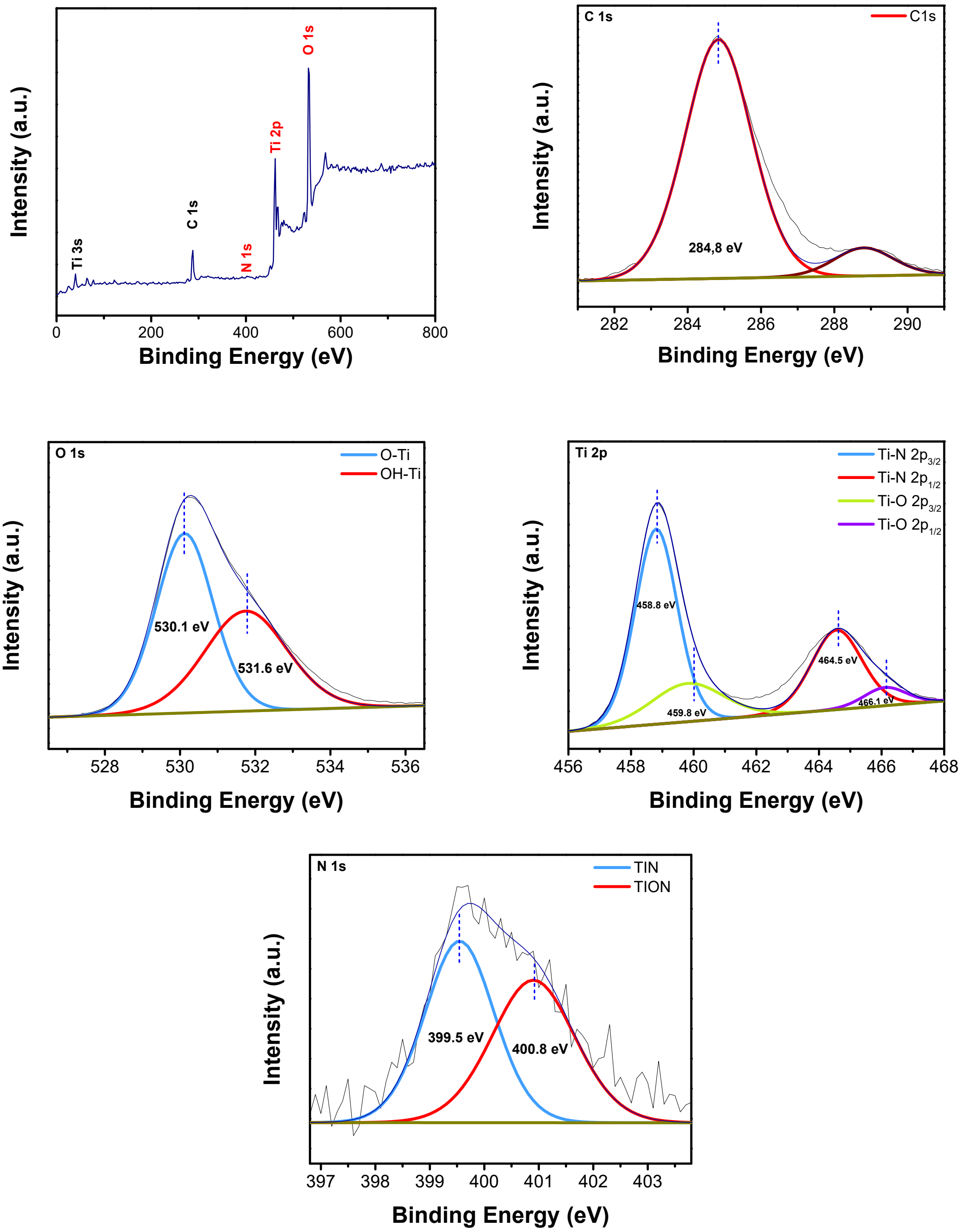

Figure S13. XPS spectra of POM-Ti_2N MXene. High-resolution XPS spectra of survey, C1s, O1s, Ti2p, and N1s respectively.

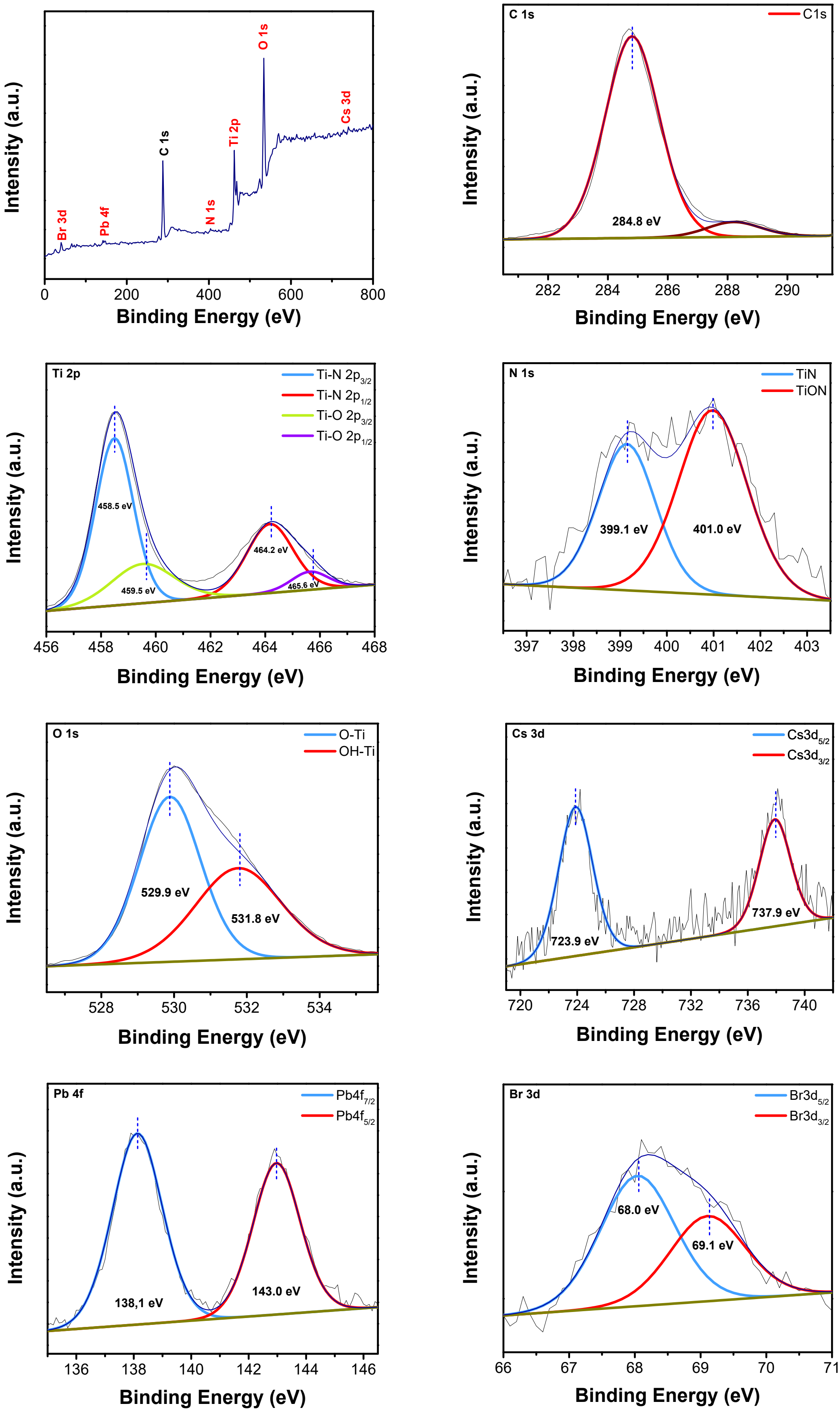

Figure S14. XPS spectra of CsPbBr$_3$@POM-Ti$_2$N MXene. High-resolution XPS spectra of survey, C1s, Ti2p, N1s, O1s, Cs3d, Pb4f and Br3d respectively.

2. DFT analysis of CO_2 and H_2 adsorption on Ti-based supports

The calculated adsorption energies and key structural features for CO_2 and H_2 on Ti_2N MXene, TiN (100) and rutile TiO_2 (110) (with and without a surface oxygen vacancy) are summarized in Table S1. On the Ti_2N MXene, molecular H_2 converged to a weakly physisorbed state (E_{ads} = -0.04 eV), with the H-H bond length remaining close to the gas-phase value and the molecule located relatively far from the surface, indicating essentially non-activated H_2. In contrast, CO_2 displayed strong chemisorption on Ti_2N (E_{ads} = -3.32 eV) in a bent configuration, consistent with substantial charge transfer and formation of surface carbonate-like species. When H_2 was artificially initialized in a dissociated configuration on Ti_2N, the optimized state was highly exothermic (E_{ads} = -7.57 eV per H_2), reflecting the strong stabilization of hydride-like species on nitride sites, although the kinetic barrier for H-H bond cleavage was not evaluated in this work.[6]

For stoichiometric rutile TiO_2 (110), CO_2 adsorption was modest (E_{ads} = -0.10 eV) and the molecule remained nearly linear and only slightly tilted towards surface Ti sites, in agreement with DFT+STM and TPD studies that report CO_2 adsorption energies in the 0.1–0.5 eV range on TiO_2 (110).[7,8] Introducing a surface oxygen vacancy (V_O) markedly strengthened CO_2 binding (E_{ads} = -1.11 eV) and led to a more strongly bent CO_2 species anchored at vacancy-associated Ti^{3+} centres, in line with the enhanced reactivity reported for defective rutile surfaces.[9] In all TiO_2 models, with and without V_O, no stable chemisorbed state was found for molecular H_2: the optimized structures relaxed to configurations where H_2 remained far from the surface with $|E_{ads}(H_2)| < 0.05$ eV, in agreement with the well-known inertness of titania towards H_2 adsorption and dissociation.[10,11]

On the rock-salt TiN (100) surface, no stable molecular H_2 adsorption state was identified. The configuration with H_2 placed near the surface relaxed to an essentially non-interacting geometry, and the corresponding adsorption energy was strongly positive (E_{ads} = +6.71eV), indicating that H_2 is effectively repelled rather than bound. This result, together with the negligible molecular H_2 binding on Ti_2N and TiO_2, is consistent with previous DFT studies on Ti nitrides and related MXene-like systems, which emphasise strong interactions with activated H and CO_2-derived species, while molecular H_2 adsorption remains unfavourable.[12,13]

Taken together with the experimental evidence that CO_2 adsorption is associated primarily with TiO_2/TiO_x domains (CO_2–TPD) and that H_2 treatment induces much easier reduction of surface oxygen species at the Ti_2N/TiO_2 interface (H_2–TPR), these DFT results support a bifunctional picture. Oxygen-deficient TiO_2/TiO_x regions (V_O/Ti^{3+}) and interfacial TiO_2/Ti_2N sites provide the main CO_2-binding and activation centres, whereas the TiN/Ti_2N nitride scaffold supplies electronic/photothermal conductivity and acts as a deep thermodynamic sink for dissociated hydrogen, rather than as a strong chemisorption site for molecular H_2.

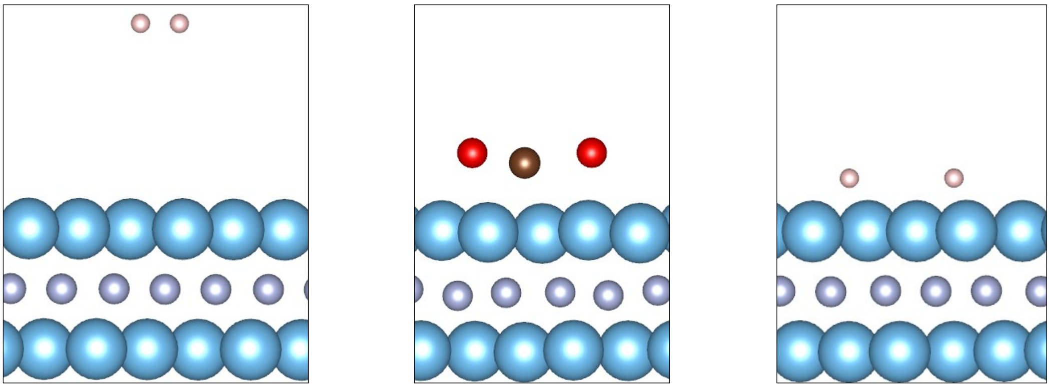

a) H_2 molecular@Ti_2N MXene b) CO_2@Ti_2N MXene c) H_2 dissociated @Ti_2N MXene

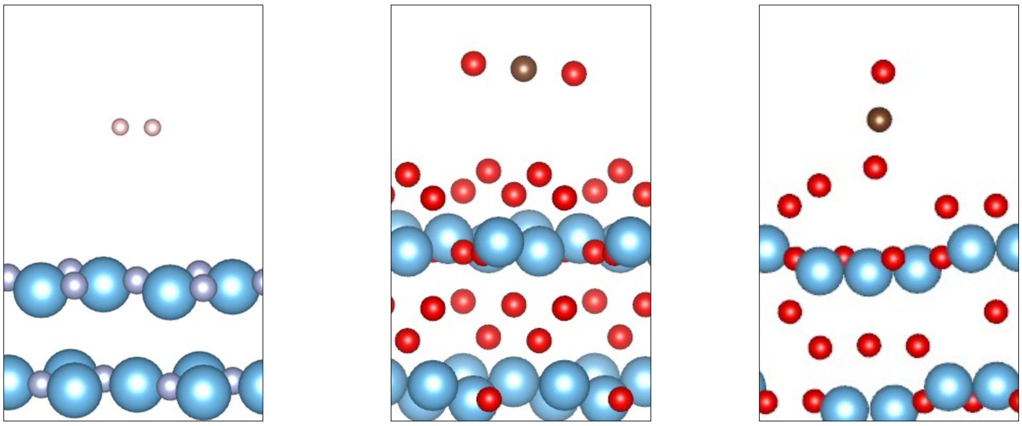

d) H_2 molecular@Ti_2N e) CO_2@TiO_2(110) f) CO_2@TiO_2+V_O(110)

Figure S15. Optimized geometries for H_2 and CO_2 adsorption on the different Ti-based surfaces

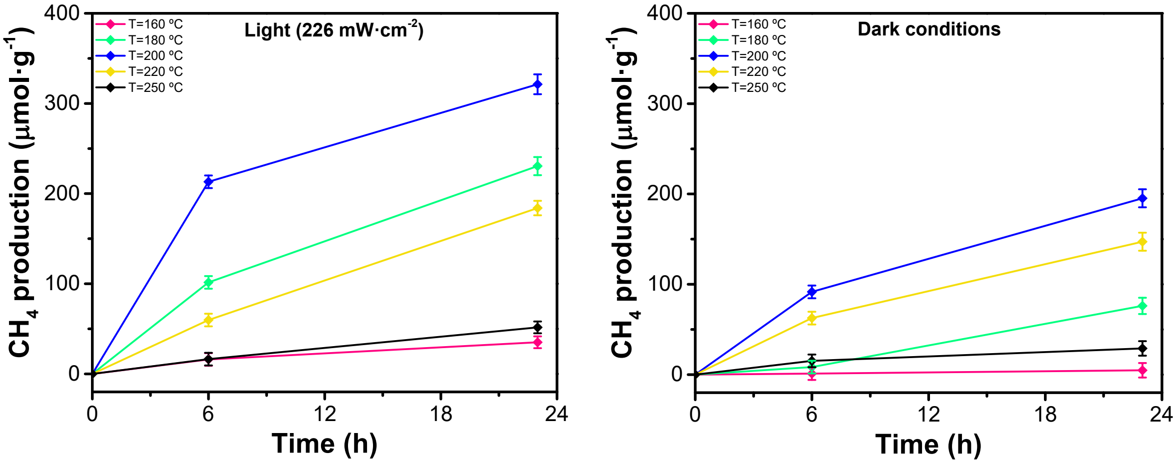

a) b)

Figure S16. a) Influence of reaction temperature on the photocatalytic CH_4 generation using $CsPbBr_3$@POM-Ti_2N MXene under simulated sunlight irradiation at 226 mW·cm^{-2} and b) under dark conditions.

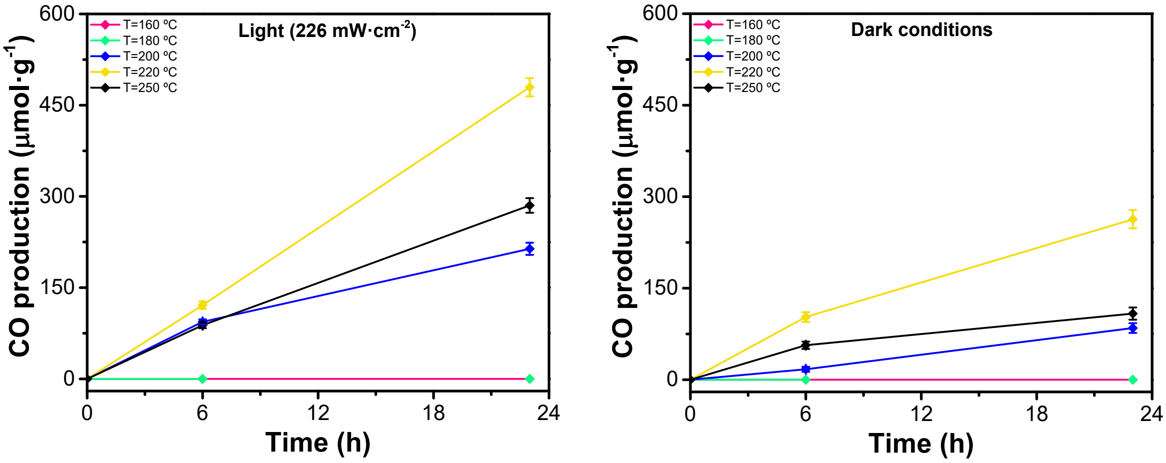

a) b)

Figure S17. a) Influence of reaction temperature on the photocatalytic CO generation using $CsPbBr_3$@POM-Ti_2N MXene under simulated sunlight irradiation at 226 mW·cm^{-2} and b) under dark conditions.

References

(1) Vighnesh, K.; Wang, S.; Liu, H.; Rogach, A. L. Hot-Injection Synthesis Protocol for Green-Emitting Cesium Lead Bromide Perovskite Nanocrystals. *ACS Nano* **2022**, *16* (12), 19618–19625. https://doi.org/10.1021/acsnano.2c11689

(2) Liu, X.; Li, Y.; Ding, H.; Chen, L.; Du, S.; Chai, Z.; Huang, Q. Topotactic Transition of Ti4AlN3 MAX Phase in Lewis Acid Molten Salt. *J. Mater.* **2023**, *9* (6), 1032–1038. https://doi.org/10.1016/j.jmat.2023.03.012

(3) Rueda-Navarro, C. M.; Abou Khalil, Z.; Melillo, A.; Ferrer, B.; Montero, R.; Longarte, A.; Daturi, M.; Vayá, I.; El-Roz, M.; Martínez-Martínez, V.; Baldoví, H. G.; Navalón, S. Solar Gas-Phase CO2 Hydrogenation by Multifunctional UiO-66 Photocatalysts. *ACS Catal.* **2024**, *14* (9), 6470–6487. https://doi.org/10.1021/acscatal.4c00266

(4) Horn, M.; Schwerdtfeger, C. F.; Meagher, E. P. Refinement of the Structure of Anatase at Several Temperatures. *Zeitschrift fur Krist. - New Cryst. Struct.* **1972**, *136* (3–4), 273–281. https://doi.org/10.1524/zkri.1972.136.3-4.273

(5) Baur, W. H.; Khan, A. A. Rutile-Type Compounds. IV. SiO2, GeO2 and a Comparison with Other Rutile-Type Structures. *urn:issn:0567-7408* **1971**, *27* (11), 2133–2139. https://doi.org/10.1107/S0567740871005466

(6) López, M.; Morales-García, Á.; Viñes, F.; Illas, F. Thermodynamics and Kinetics of Molecular Hydrogen Adsorption and Dissociation on MXenes: Relevance to Heterogeneously Catalyzed Hydrogenation Reactions. *ACS Catal.* **2021**, *11* (21), 12850–12857. https://doi.org/10.1021/acscatal.1c03150

(7) Sorescu, D. C.; Lee, J.; Al-Saidi, W. A.; Jordan, K. D. CO2 Adsorption on TiO2(110) Rutile: Insight from Dispersion-Corrected Density Functional Theory Calculations and Scanning Tunneling Microscopy Experiments. *J. Chem. Phys.* **2011**, *134* (10), 104707. https://doi.org/10.1063/1.3561300

(8) Yin, W. J.; Krack, M.; Wen, B.; Ma, S. Y.; Liu, L. M. CO2 Capture and Conversion on Rutile TiO2(110) in the Water Environment: Insight by First-Principles Calculations. *J. Phys. Chem. Lett.* **2015**, *6* (13), 2538–2545. https://doi.org/10.1021/acs.jpclett.5b00798

(9) Sorescu, D. C.; Lee, J.; Al-Saidi, W. A.; Jordan, K. D. Coadsorption Properties of CO2

and H 2O on TiO 2 Rutile (110): A Dispersion-Corrected DFT Study. *J. Chem. Phys.* **2012**, *137* (7), 74704. https://doi.org/10.1063/1.4739088

(10) Raupp, G. B.; Dumesic, J. A. Adsorption of Carbon Monoxide, Carbon Dioxide, Hydrogen, and Water on Titania Surfaces with Different Oxidation States. *J. Phys. Chem.* **2002**, *89* (24), 5240–5246. https://doi.org/10.1021/j100270a024

(11) Wei, B.; Calatayud, M. Hydrogen Activation on Anatase TiO2: Effect of Surface Termination. *Catal. Today* **2022**, *397–399*, 113–120. https://doi.org/10.1016/j.cattod.2021.11.020

(12) Jurado, A.; Ibarra, K.; Morales-García, Á.; Viñes, F.; Illas, F. Adsorption and Activation of CO2 on Nitride MXenes: Composition, Temperature, and Pressure Effects. *ChemPhysChem* **2021**, *22* (23), 2456–2463. https://doi.org/10.1002/cphc.202100600

(13) Morales-Salvador, R.; Gouveia, J. D.; Morales-García, Á.; Viñes, F.; Gomes, J. R. B.; Illas, F. Carbon Capture and Usage by MXenes. *ACS Catal.* **2021**, *11* (17), 11248–11255. https://doi.org/10.1021/acscatal.1c02663